Supplementary: Single-exposure holographic lithography of ultra-high aspect-ratio microstructures

Dajun Lin[1], Brian Baker[2], Rajesh Menon[1,*]
[1]Department of Electrical & Computer Engineering, University of Utah, Salt Lake City, 84112, USA
[2]Utah Nanofab, University of Utah, Salt Lake City, UT 84102, USA

Contents

Notes S1 to S17

Figs. S1 to S14

Note S1: Optical contrast definition

Optical contrast in lithography refers to how distinctly the projected intensity distribution separates bright (exposed) and dark (unexposed) regions at the photoresist plane. The optical contrast K is defined as:

$$K = \frac{\langle I \rangle_t - \langle I \rangle_b}{\langle I \rangle_t + \langle I \rangle_b}$$

Where $\langle I \rangle_t = \frac{1}{|\Omega_t|} \iint_{\Omega_t} I(x,y)dxdy$ refers to the average intensity in target region, $\langle I \rangle_b = \frac{1}{|\Omega_b|} \iint_{\Omega_b} I(x,y)dxdy$ refers to the average intensity in background region.

Note S2: Diffraction distribution of the binary photomask and hologram phase mask

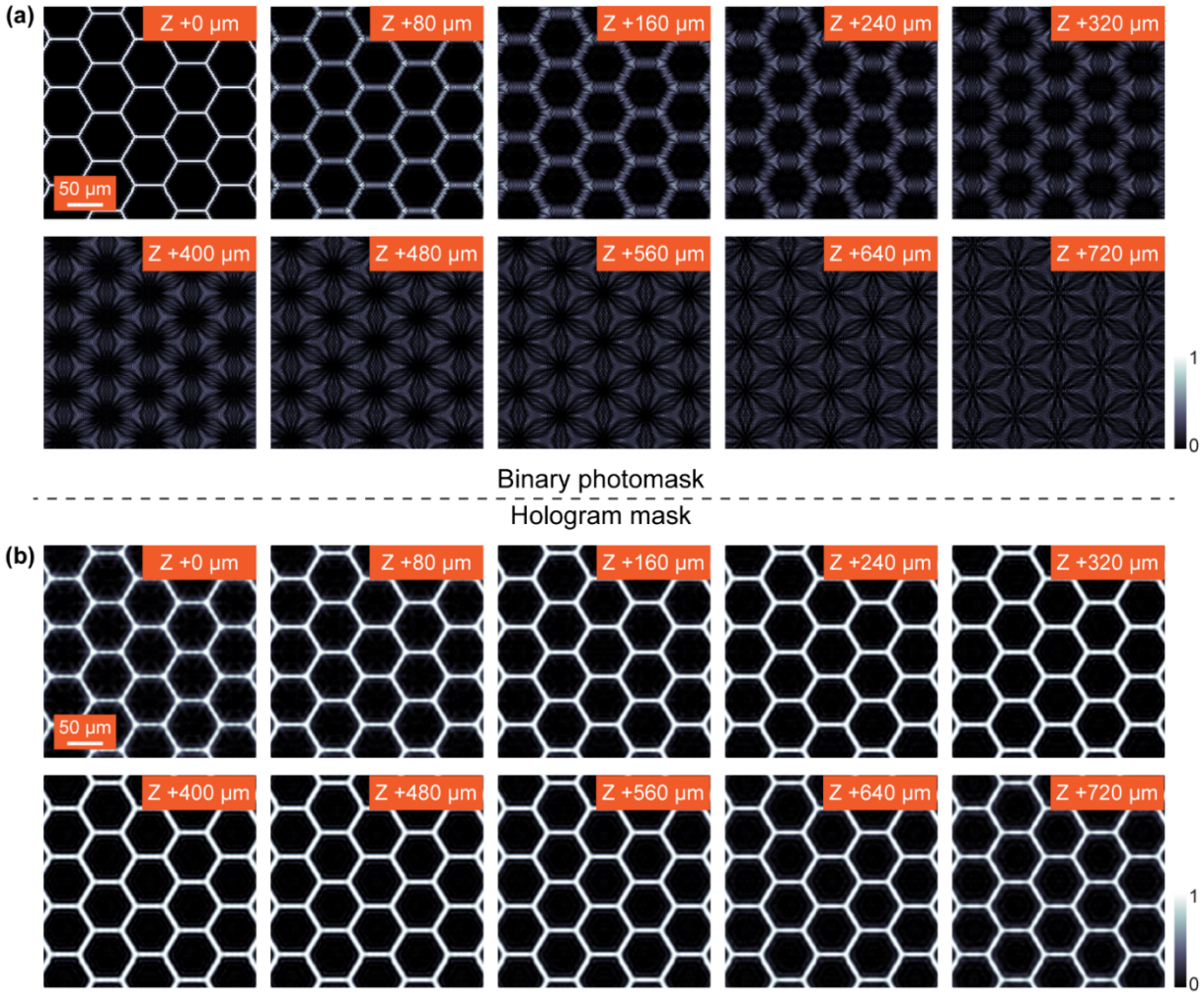

Fig. S1 Diffraction distribution of the binary photomask (a) and hologram phase mask in (b).

Note S3: Experimental measured hologram mask intensity distribution

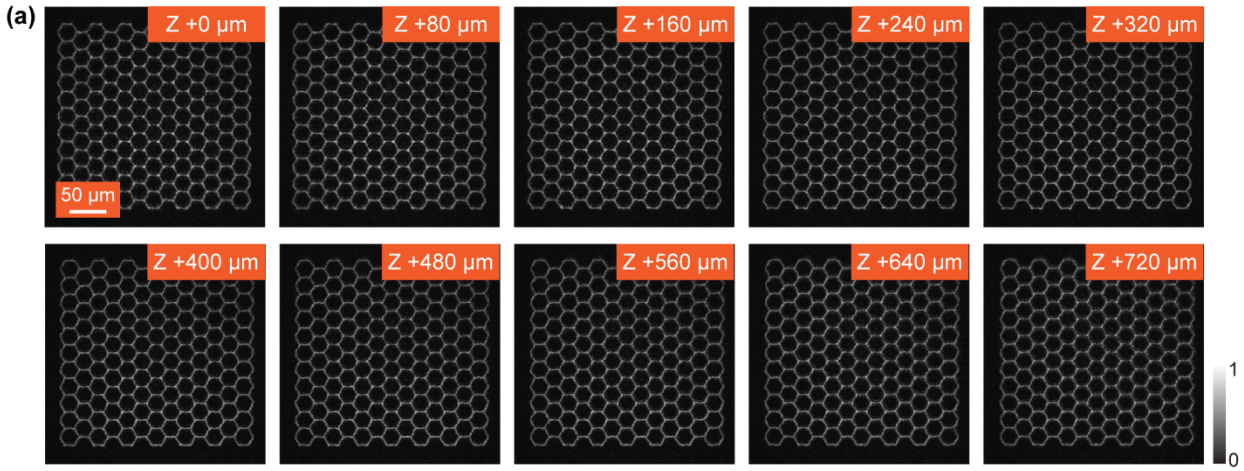

Fig. S2 Experimental measured hologram mask intensity distribution.

Note S4: Inverse design of the hologram mask

To generate the desired volumetric exposure light field, we inverse designed a computer-generated hologram (CGH) that preserves the target intensity distribution throughout the specified 3D region. A fully differentiable model is implemented in TensorFlow (v2.20.0, Google Inc.) to optimize the hologram phase distribution φ. The mask is illuminated by a plane wave with complex field $t_0 = \exp(i\phi(x, y))$, and forward propagation is performed using the angular spectrum method (ASM), The propagated field at axial position Z_i is expressed as $H^{(Z_i)}\{t_0\}$, yielding the intensity distribution

$$I^{Z_i} = abs(H^{Z_i}\{t_0\})^2$$

The intensities are compared with the target distribution T^{Z_i}, derived from computer-aided design (CAD) slices. The loss function is defined as the mean squared error

$$\mathcal{L} = \frac{1}{N}\sum_{i=1}^{N}(I^{Z_i} - T^{Z_i})^2$$

which is fully differentiable and enables gradient-based optimization. During training, the hologram phase is iteratively updated until the reconstructed volumetric intensity converges to the target distribution.

The phase optimization requires about 25 minutes on a desktop workstation with an NVIDIA 3060 GPU and an Intel i7-12700 CPU. After convergence, the optimized phase profile is converted to a physical height distribution according to

$$h(x, y) = \frac{\lambda}{2\pi\Delta n}\emptyset(x, y)$$

where λ is the exposure wavelength and Δn is the refractive index contrast between the photoresist and the air.

Note S5: Mask fabrication and characterization

The hologram mask was fabricated using grayscale optical lithography. A 2-inch diameter soda-lime glass wafer was spin-coated with a positive-tone photoresist (MICROPOSIT S1813 G2) at 1500 rpm for 60 s, followed by a soft bake on a hotplate at 110 °C for 2 min. A calibration step was performed to establish the relationship between laser dose and resist height. The phase mask pattern was defined using a laser pattern generator (DWL66+, Heidelberg Instruments GmbH). After exposure, the sample was post-baked at 50 °C for 1 min, developed for 1 min in AZ developer (1:1 dilution), and rinsed in deionized (DI) water. The designed and fabricated hologram phase masks are shown in Fig. S4.

The mask height distribution was characterized using a confocal microscope (Olympus LEXT OLS5000). Representative micrographs and the measured height profile are shown in Fig. S3.

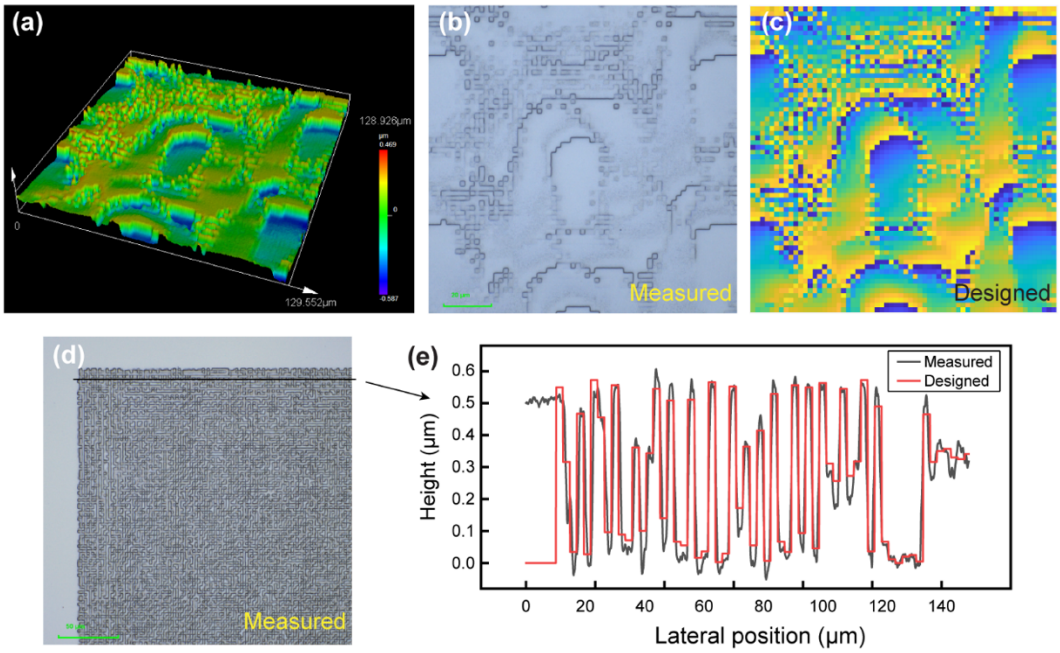

Fig. S3 Fig. S3 Mask characterization. (a-b) Optical micrograph of the mask at 100× magnification, with the corresponding design comparison shown in (c). (d) 100× micrograph of the mask edge, together with a comparison between the designed and measured height profiles in (e).

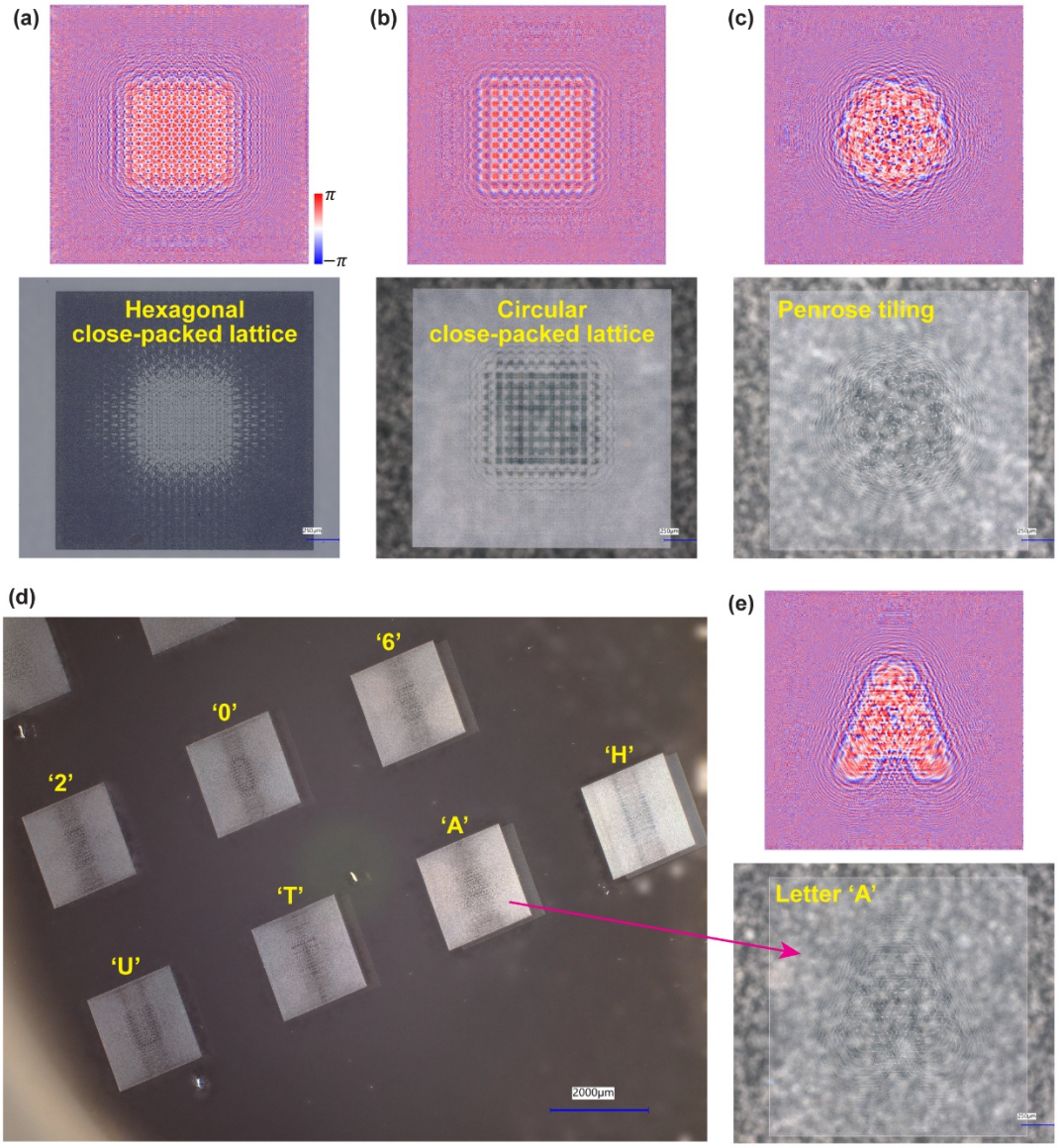

Fig. S4 Designed and fabricated hologram phase masks. The designed and fabricated hexagonal close-packed (HCP) lattice mask in (a), the circular close-packed lattice in (b), the Penrose tilting mask in (c), and letter 'a' mask in (e). (d) shows several masks fabricated on the same 2-inch soda-lime glass wafer.

Note S6: Custom-built single-exposure lithography system

Exposures were performed using a custom-built single-exposure lithography system, schematically illustrated in Fig. 3a. A 405 nm diode laser (100 mW; Edmund Optics, #19-462) was spatially filtered and collimated using lenses L1 and L2 in combination with a 25 μm pinhole (P25K05 Thorlabs) to generate uniform illumination. The beam passed through a mechanical shutter (LS2, Vincent Associates) and was redirected by mirrors (M_1, M_2) toward the aperture and hologram mask. The mask modulated the optical field to reconstruct the target volumetric intensity

distribution within the SU-8 photoresist. Shutter timing was controlled using Python (v3.7.2). The mask, SU-8 wafer holder, and CMOS camera were mounted on a three-axis motion stage (version) for precise positioning, and both the mask and wafer holders incorporated additional two-axis lateral adjustment for fine alignment (alignment protocol see Note S7). The CMOS camera was integrated with a 1:1 magnification relay imaging system (1:1 Matched Achromatic Pair, f1 = 75.0 mm, f2 = 75.0 mm, MAP107575-A, Thorlabs), enabling non-contact monitoring of both the holographic intensity distribution and the axial position of the SU-8 wafer through conjugate-plane imaging.

The laser power was measured to be ~17 mW before the aperture. The beam diameter was intentionally larger than the mask size to ensure uniform illumination. After passing through the 2 × 2 mm square aperture, the transmitted power was measured to be 4.8 mW, corresponding to an illumination intensity of approximately 120 mW/cm² at the mask plane.

Note S7: Alignment protocol

The 3D holographic intensity pattern is designed to appear 20 mm above the hologram mask. The optics rely monitoring system is applied, instead of ring shim, for the precise lateral (X/Y) and axial (Z) alignment. The axial and later alignment process are based on the optical setup shown in Fig. S5a and Note S6, the square mask, hologram mask, SU-8 wafer, and monitoring system are mounted on 4 individual translation stages for movement. A neutral density (ND) filter is additionally applied before mask to prevent dose accumulation to the photoresist. The alignment can be divided to three steps, shown in Fig. S5a,

Step 1: Position monitoring system (CMOS and optics rely). The mask is initially positioned to project the 3D intensity distribution. A CMOS-based position monitoring system with relay optics was used to observe the exposure plane. The monitoring module was axially translated to image the top surface of the 3D intensity distribution, while the SU-8 photoresist remained in place to maintain the optical path length.

Step 2: SU-8 wafer axial alignment. After Step 1, the monitoring system position was fixed, and the mask was moved out for photoresist wafer alignment. The upper surface of the photoresist wafer was marked and translated to the focal plane. In-focus and out-of-focus images are shown in Fig. 3b. Owing to the translucency of the markers, sharp edges are visible at focus, whereas pronounced contour patterns emerge when defocused due to light propagation.

Step 3: Mask lateral alignment. The mask was translated back for subsequent later alignment. Due to the Gaussian intensity profile of the laser beam, the mask and square aperture were carefully aligned to ensure uniform dose distribution. The aperture can be placed either before or after the mask to block unwanted surrounding exposure and stray light.

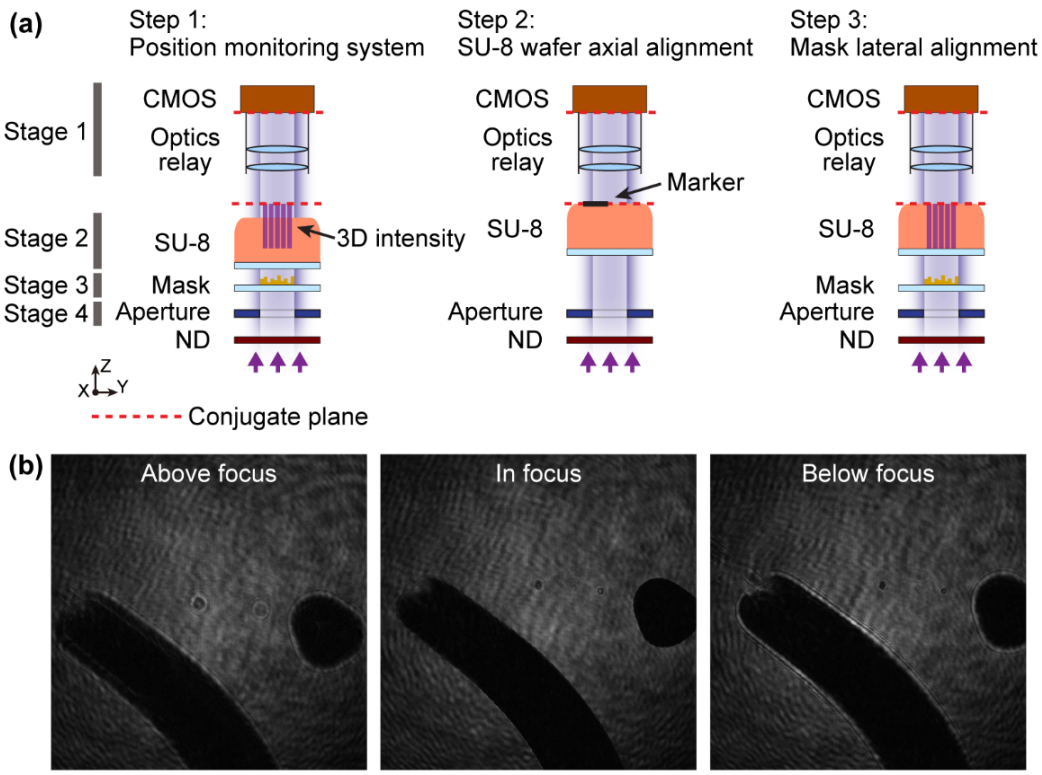

Fig. S5 Mask-Resist alignment protocol. (a) Experiment setup illustration. Stage 1: Manual 3-axis stage. Stage 2: Motorized 3-axis stage. Stage 3: Manual 2-axis stage (X/Y). Stage 4: Manual 3-axis stage. (b) Monitoring images show axial alignment of the mask on SU-8 above focus, at focus, and below focus.

Note S8: Comparison with two-photon polymerization lithography

For comparison, we fabricated the same hexagonal-cell lattice structure using a high-resolution two-photon polymerization (2PP) 3D nano printing, Nanoscribe Photonic Professional GT2. A 10X objective lens and IP-Q photoresist were used, providing 2 µm transverse and 10 µm axial resolution. The structure was sliced with a 2 µm layer spacing and a 1 µm hatching distance. The galvo scanner was used for lateral scanning, and the microscope Z-drive for axial motion. The laser power was set to 90%, with a solid scan speed of 100,000 µm s^{-1}. Following exposure, the sample was developed in PGMEA for 40 min and rinsed in IPA for 10 min.

The 2PP-fabricated structure (Fig. S6a–c) has overall dimensions of 800 × 800 × 720 $µm^3$, identical to those produced using our single-exposure approach (Fig. S6d–f). Fabrication by 2PP required 22 min, corresponding to a volumetric throughput of 1.13 mm^3 h^{-1}. In contrast, our single-exposure method achieves comparable 4-µm feature resolution at a 66-fold higher speed, with an effective throughput of 75 mm^3 h^{-1}. Compared with other axially stacked additive manufacturing technologies, our single-exposure approach yields superior surface morphology and mechanical integrity, see Fig. S6b and e. The slight bending observed near the top of our printed structures arises from the PEB thermal process, which is required for SU-8 but not for 2PP fabrication.

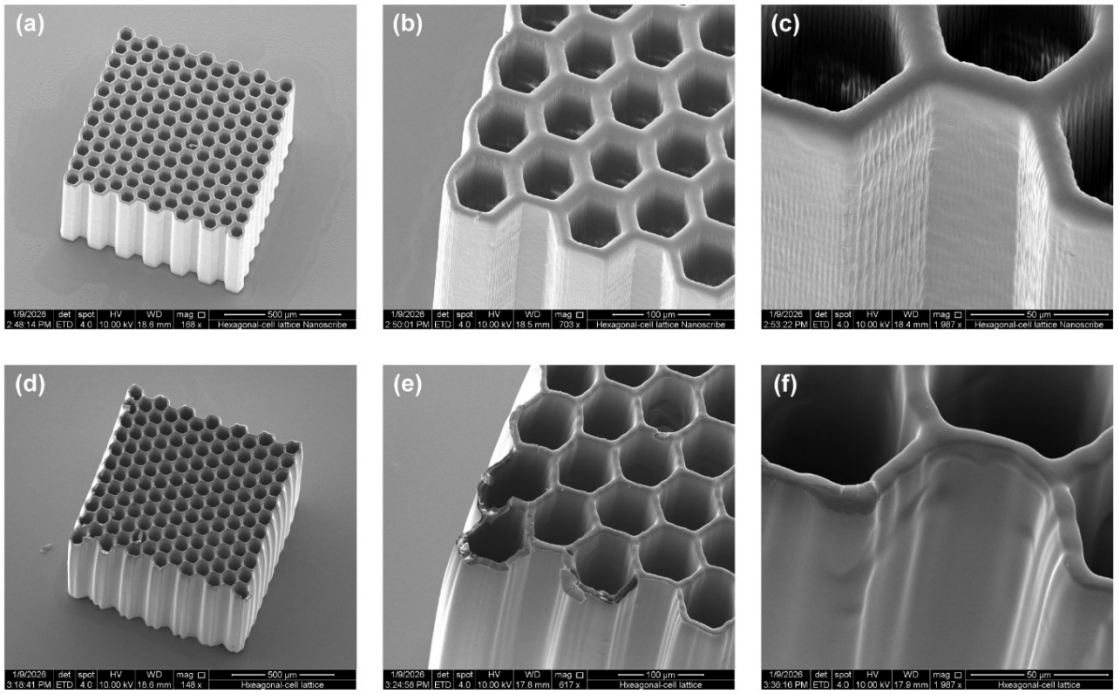

Fig. S6 Comparison with other lithography methods. (a-c) Hexagonal-cell lattice structure fabricated using Nanoscribe two-photon polymerization (2PP). (d-f) Hexagonal-cell lattice structure fabricated by inverse-designed hologram mask.

Note S9: SEM measured structures

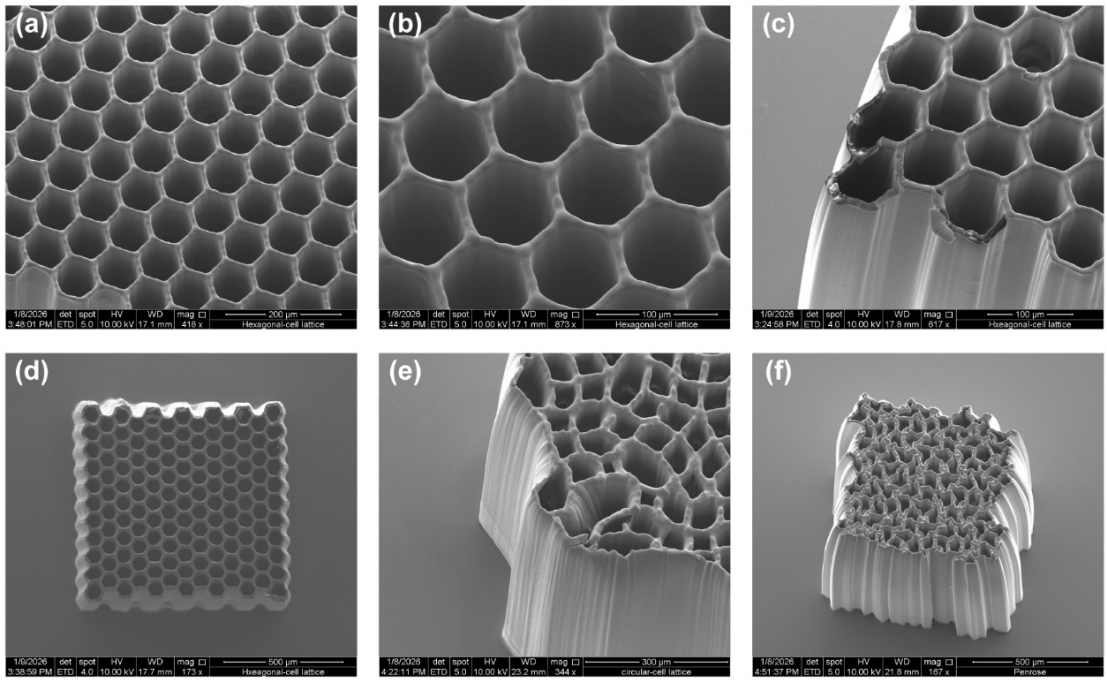

Fig. S7 Additional SEM measured structures. (a-c) Tilted view of the hexagonal close-packed (HCP) lattice. (d) Top view of the HCP lattice. (e-f) Penrose tiling structures.

Note S10: Enhancing complexity of printed microstructures via stepped exposures

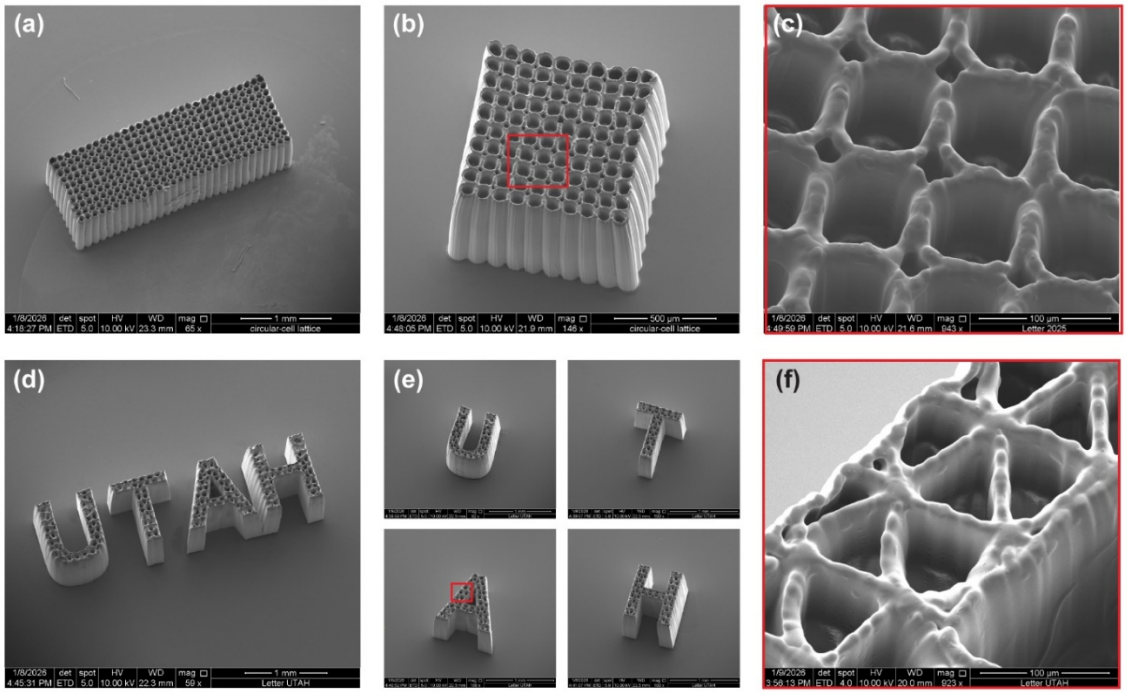

Fig. S8 Enhancing complexity of printed microstructures via stepped exposures. (a-c) Large lattice and single-exposed lattice. (d-f) Letter 'UTAH' and its individual letters.

Note S11: Enhancing complexity of printed microstructures via tilted and overlapping exposures

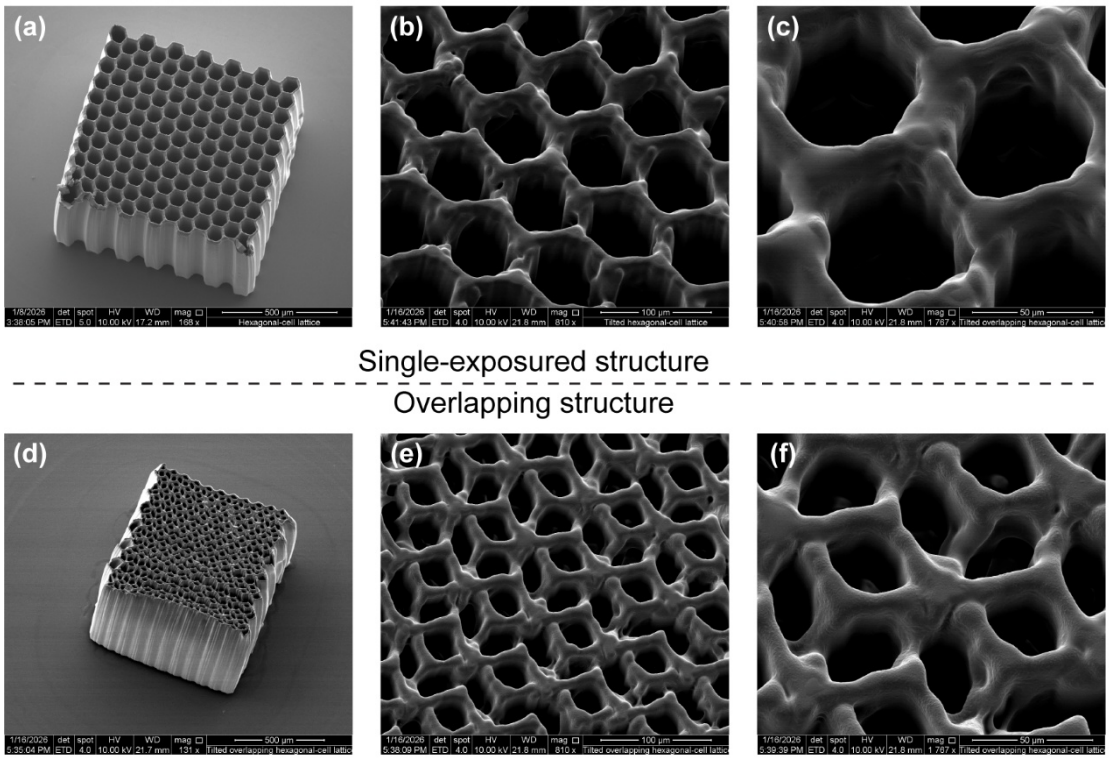

Fig. S9 Single-exposured structure (a) and overlapping structures (b).

Note S12: Various dose testing and printing resolution

The intensity profile for the 3D reconstructed patterns, is actually showing edge blurring effects. This is because the optical imaging system is mathematically a linear shift-invariant (LSI) low-pass filter, and the image is the convolution of the object with the point spread function (PSF). For a coherent-incoherent general system:

$$I_{\text{image}}(x, y) = I_{\text{object}}(x, y) * \text{PSF}(x, y)$$

The PSF function is defined by system NA with a diffraction-limited full-width of half-maximum (FWHM) of $FWHM \approx \lambda/2NA \approx 4$ μm. As we can see the cross-sectional the intensity in Fig. S10a, it is Gaussian-shaped like, could leads to printed wall width dose-dependent. To study the optimize exposure for thick resist dose, we tested the dose required for 720 μm thickness SU-8 by the system shown in Fig. S10, with various exposure times from 4 to 32 sec. The structures first appeared at an exposure time of 12 s, corresponding to a dose threshold of approximately 8.4 J cm^{-2} at 405 nm. At this threshold, the printed features exhibited extremely thin wall thicknesses of 4.71 ± 0.34 μm and naturally bent after development, indicating poor mechanical integrity at high aspect ratios (exceeding 150:1). As the exposure time increased from 12 s to 32 s, the measured wall thickness increased continuously, reflecting progressive overexposure and polymerization of the lower-intensity Gaussian tails. The measured hexagon ring width is increased from 4.71 ± 0.34

μm (12 s) to 10.20 ± 0.74 μm (32 s), see Fig. S10b. The resulting structures exhibited significantly improved mechanical robustness.

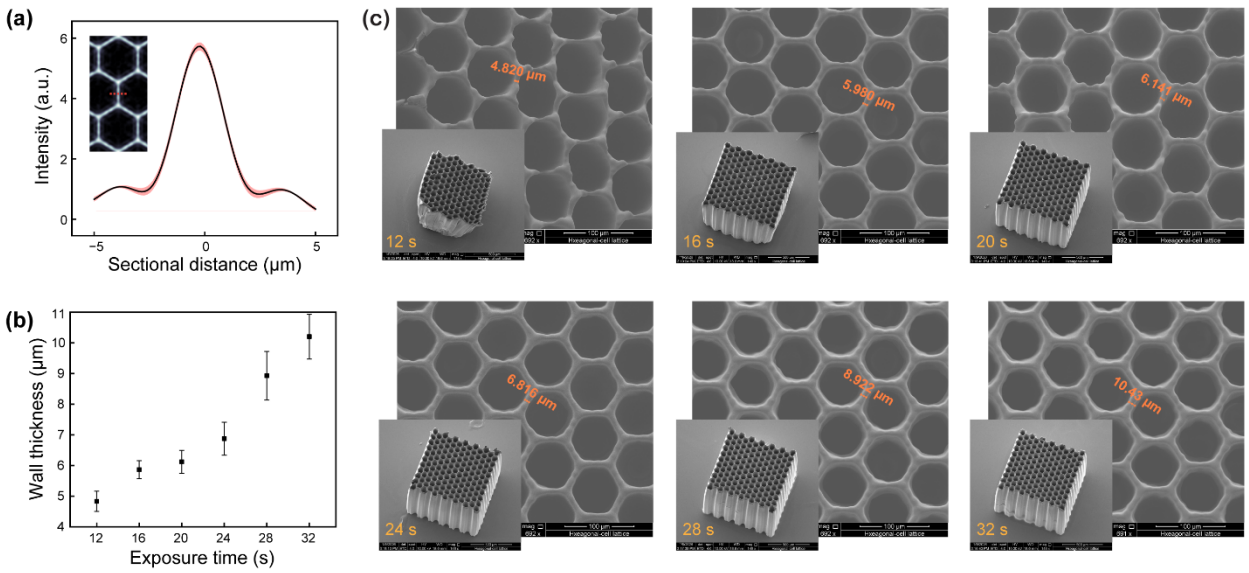

Fig. S10 Various dose testing and printing resolution. (a) Cross-sectional intensity of the designed hexagonal-cell lattice, tested at 100 μm above the bottom plane. The Gaussian-like intensity profile indicates that the printed wall width is dose-dependent. (b) Measured hexagonal ring width as a function of exposure time (12–32 s). (c) SEM images of hexagonal-cell lattices fabricated with exposure times from 12 to 32 s.

Note S13: Aspect-ratio limitation analysis

We numerically investigate the aspect ratio limitation of the hexagonal-cell microstructure by varying the target structure depth from 0 to 6400 μm in 800 μm increments. The hexagonal cell diameter is fixed at 80 μm. In cross section, the hexagonal ring exhibits a Gaussian-like intensity profile, and the ring thickness is quantified by its FWHM values. At zero designed depth, corresponding to a single-layer pattern, the structure achieves the best lateral resolution with a minimum FWHM of 6 μm, approaching the Airy disk limit determined by the system NA (0.05) and 20 μm gap distance. As the target depth increases, the FWHM progressively broadens (Fig. S11a), reaching ~16 μm at 6400 μm depth, approximately 2.5X larger than the diffraction-limited value.

This broadening resembles the quasi diffraction-free behavior of a Bessel-like field generated by conical wave superposition, where the central lobe expands over extended propagation distances. Simultaneously, increased side-lobe energy induces interference within individual hexagonal patterns, degrading optical contrast (Fig. S11b).

The single-layer pattern exhibits the highest optical contrast (K=0.92). With increasing depth, the contrast decreases rapidly beyond the designed region and can become negative, with partial

recovery attributed to the Talbot effect. The depth-averaged contrast decreases monotonically as the structure becomes deeper. At 6400 μm, the average contrast reduces to K~0.5, insufficient for reliable photolithographic patterning. Representative intensity distributions are shown in Fig. S10d. We further evaluate the influence of pattern density by varying the hexagonal diameter (40–160 μm) at a fixed depth of 3200 μm (Fig. S11c). Larger cells exhibit improved contrast due to reduced side-lobe interference, indicating that lower-density patterns are more robust for high-aspect-ratio fabrication.

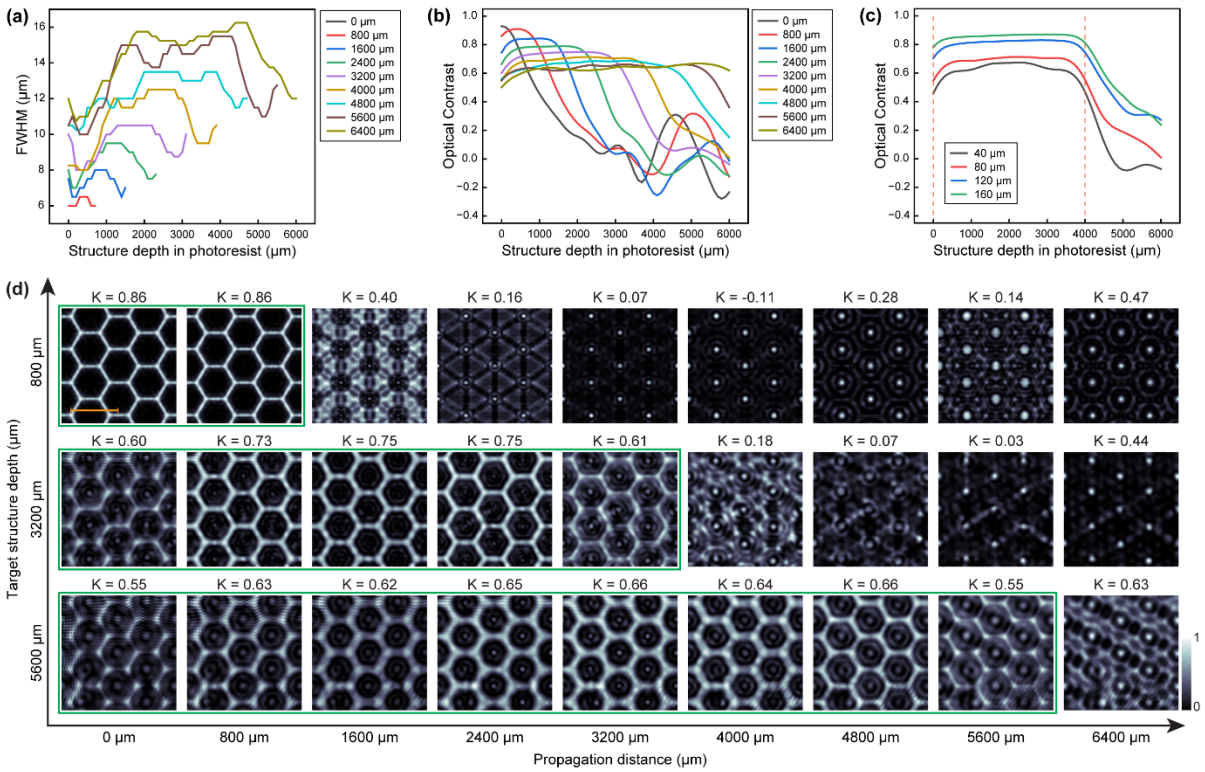

Fig. S11 Aspect ratio limitation analysis. The hexagonal ring thickness (FWHM) and optical contrast were evaluated as a function of target structure depth, varied from 0 to 6400 μm in 800 μm increments. (a) Ring thickness versus target structure depth, quantified by FWHM. (b) Optical contrast versus target structure depth. (c) Optical contrast as a function of hexagonal diameter at a fixed target structure depth of 3200 μm. (d) Simulated intensity distributions corresponding to depths from 0 to 6400 μm.

Note S14: Capillary flow through high-aspect ratio hollow lattice

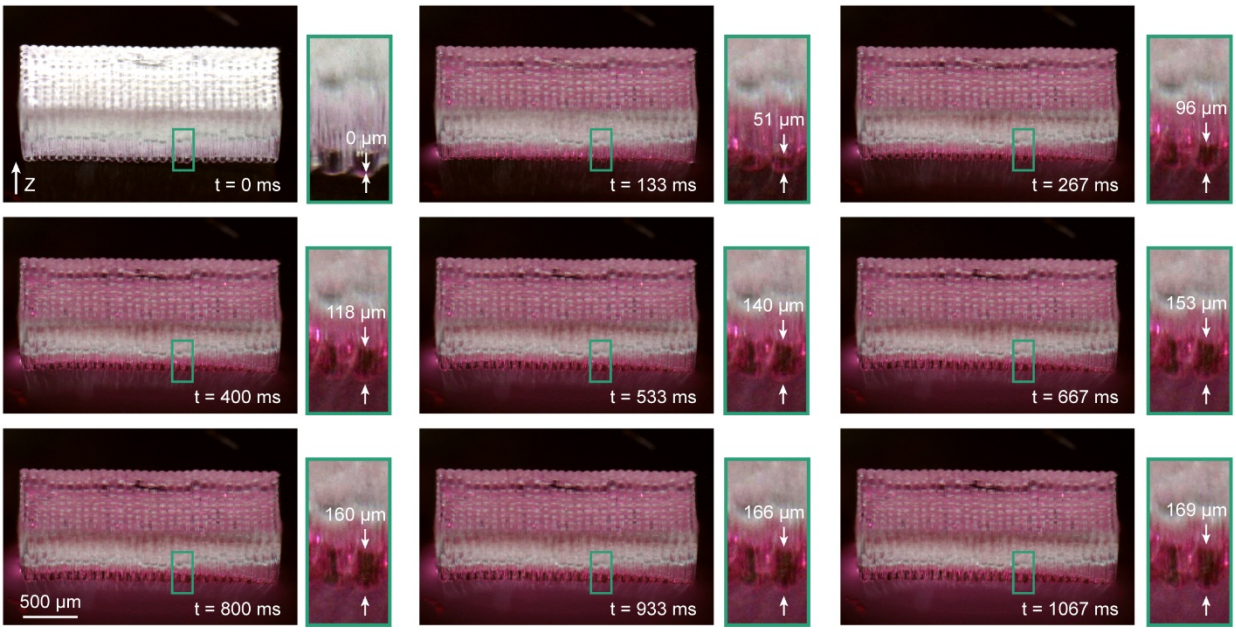

Fig. S12 Capillary flow through high-aspect ratio hollow lattice.

Note S15: Nanoindentation

To evaluate the mechanical properties of the printed HCP structure, uniaxial micro-compression tests were performed using a nano-indenter µTest Rig (µTR, MTR-3-XR) equipped with a 2 µm diameter flat punch tip. The testing frame operates inside a Teneo SEM, enabling in situ mechanical testing and simultaneous SEM imaging. The experimental configuration is shown in Fig. S13a.

The indenter motion was controlled by a piezo actuator driven by a voltage range of 0–150 V, enabling precise displacement control. The applied force was measured using a strain-gauge load cell, with a maximum recorded load of 531.14 g. Load–displacement data were recorded during monotonic compression, reaching a maximum displacement of 502.5 µm, corresponding to 62.81% of the initial specimen height.

The loading process can be divided into four stages. In the first stage (0–125.4 µm), displacement was driven by the piezo actuator at a constant speed of 23 nm s^{-1}. In the second stage (125.4–216.8 µm), compression was controlled by the XYZ mechanical stage, with the sample moving toward a fixed tip in 10 µm steps at a speed of 1 µm s^{-1}. The third stage (216.8–502.5 µm) followed the same stepwise motion with a speed of 1.25 µm s^{-1}. The final stage corresponds to unloading, during which the tip retracted and the load decreased. The measured load (red) and displacement (blue) as functions of time are shown in Fig. S13b.

The engineering stress–strain response was calculated from the measured load and displacement. The engineering stress σ was defined as:

$$\sigma = \frac{F}{A_0}$$

where F is the applied load and A_0 is the initial cross-sectional area of the specimen (800 × 720 μm²). The engineering strain ε was defined as:

$$\varepsilon = \frac{\Delta L}{L_0}$$

where L_0 = 800 μm is the initial specimen height, and ΔL is the axial displacement after first contact between the indenter and the specimen (ranging from 0 to 502.5 μm). The resulting stress–strain curve is shown in Fig. S13c. The Young's modulus E was extracted from the slope of the initial linear elastic region of the stress–strain curve:

$$E = \frac{d\sigma}{d\varepsilon}$$

Figure S13d shows manually aligned in situ SEM images capturing the progressive compression of the HCP structure. At small strain (ε < 9%), deformation is predominantly elastic. The cell walls undergo uniform bending without visible fracture, and the stress–strain curve remains linear, corresponding to an effective Young's modulus of approximately 5.7 GPa.

At approximately 9% strain, deviation from linearity indicates the onset of structural instability. Initial failure originates near the left side of the specimen. This asymmetric failure is attributed to imperfect contact between the flat punch and the sample surface. Because the top surface of the printed structure is not perfectly planar, localized stress concentration occurs at the initial contact region, leading to premature buckling and fracture of the left-side cell walls.

With increasing compression, progressive collapse propagates downward along the left column of cells. The right side of the structure, which experiences more uniform load transfer, remains structurally intact for a longer period. This sequential cell-wall buckling results in the serrated stress–strain behavior observed in Fig. S13c.

At higher strain levels, significant crushing and densification occur. In the final frame (bottom-right image), the indenter begins unloading. A slight elastic recovery is observed on the right side of the structure, as evidenced by partial rebound of intact cell walls. In contrast, the left side remains permanently deformed due to irreversible fracture and plastic collapse.

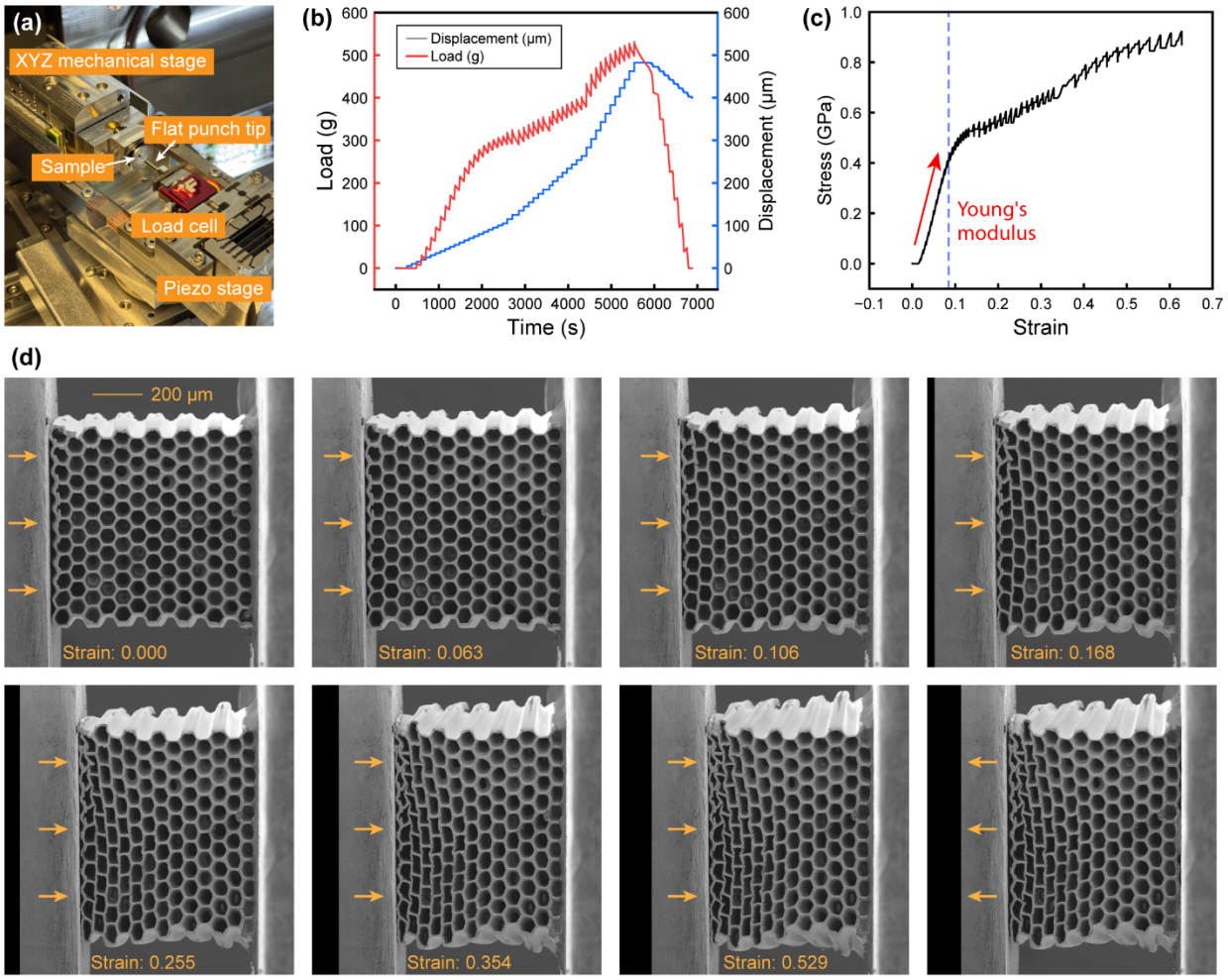

Fig. S13 In situ SEM compression characterization of 3D printed HCP structure. (a) Experimental configuration of the micro-test rig inside the SEM, showing the piezo stage, load cell, flat punch tip, and testing sample. (b) Measured load (red) and displacement (blue) as a function of time during compression. (c) Corresponding engineering stress–strain curve derived from load–displacement data, with Young's modulus extracted from the linear elastic regime (dashed line). (d) Time-resolved SEM images showing progressive deformation of the hexagonal lattice under increasing compressive strain. Arrows indicate regions of localized bending and densification. Scale bar: 200 μm. Arrow is the indenter moving direction.

Note S16: Printing resolution resolution

The printing resolution is directly related to the optical resolution of the reconstructed intensity field. In an optical system, the resolution is determined by the numerical aperture (NA) and the operating wavelength, where

$$NA = nsin(\theta) \approx \sin(\theta)$$

In this work, the mask size is 2 mm, and the reconstructed 3D intensity field is located 20 mm away from the mask. Therefore, the system NA is approximately 0.05. The theoretical full width at half maximum (FWHM) can be estimated as

$$FWHM = \lambda/2/NA$$

In our case, the FWHM, and thus the printing resolution, is approximately 4 μm.

The printing resolution can be improved by increasing the system NA. Two different limits should be considered: the aperture-limited resolution, NA_{ap}, and the pixel-pitch-limited resolution, NA_{pp}, depending on the distance between the image plane and the mask plane.

If the entire mask of size D contributes to a point in the image plane at distance d, the aperture-limited NA is

$$NA_{ap} \approx sin\theta \approx \frac{\frac{D}{2}}{\sqrt{d^2 + \left(\frac{D}{2}\right)^2}} \approx \frac{D}{2d} \ (d \gg D)$$

When the 3D object is brought closer to the mask, the pixelation of the mask becomes important. A pixelated mask cannot generate arbitrarily large diffraction angles. Since the smallest period that can be represented is on the order of $2p$, where $p$is the pixel pitch, the maximum transverse spatial frequency is limited, and the corresponding pixel-pitch-limited NA can be written as

$$NA_{pp} \approx sin\theta \approx \frac{\lambda}{2p}$$

The actual usable NA is approximately the smaller of these two limits:

$$NA_{eff} \approx \min\left(NA_{ap}, NA_{pp}\right)$$

In the future, the resolution can be further improved by using a mask with a smaller feature size and by reducing the gap distance between the reconstructed 3D intensity field and the mask. For example, a mask with a pixel pitch of 500 nm can support an NA of about 0.4, corresponding to a printing resolution of approximately 500 nm .

Note S17: Printed standalone cylindrical micropillar structures

The 10 × 10 cylindrical micropillar array was designed with a radius of 24 μm and a height of 720 μm, yielding an aspect ratio of 15:1. The middle layer of the designed intensity distribution and the corresponding mask are presented in Fig. S14. The micropillar structures were evaluated under varying exposure doses, with exposure times from 20 to 40 s in 4 s increments. At an exposure time of 20 s, the structure collapsed, and some pillars detached from the substrate, likely due to reduced adhesion at the pillar base during the extended development process. This limitation may be alleviated by using a different substrate, such as Silicon wafer, which typically provides better

adhesion for SU-8 than glass. In contrast, the micropillar structures fabricated at 32 s and 40 s exhibited improved mechanical stability and well-defined geometries, with only slight pillar bending observed.

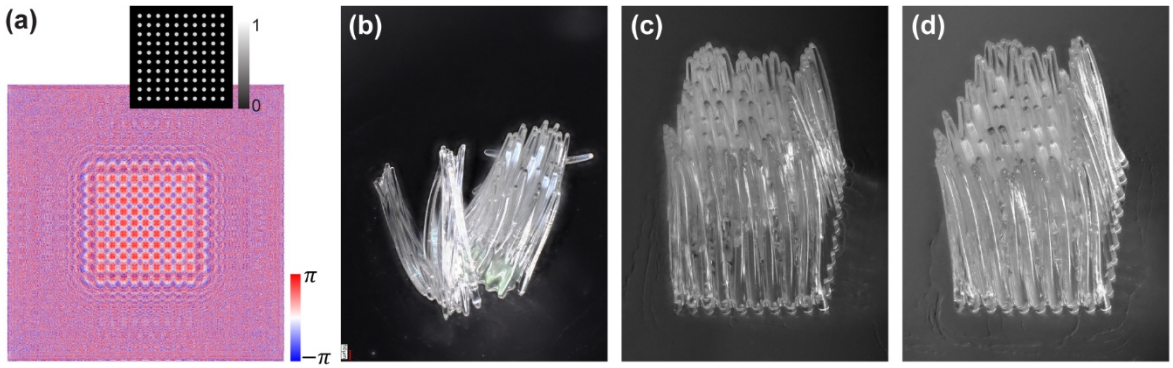

Fig. S14 Printed standalone cylinder structure. (a) Designed intensity pattern and corresponding phase mask for the standalone micropillar structure. (b–d) Fabricated micropillar structures produced with exposure times of 20, 32, and 36 s, respectively.